2D Materials

PAPER • OPEN ACCESS

Band alignments, conduction band edges and intralayer bandgap renormalisation in $MoSe_2/WSe_2$ heterobilayers

To cite this article: A J Graham *et al* 2024 *2D Mater.* **11** 045021

IOP Publishing 2D Mater. 11 (2024) 045021 https://doi.org/10.1088/2053-1583/ad7b51

2D Materials

RECEIVED
11 June 2024

REVISED
9 August 2024

ACCEPTED FOR PUBLICATION
16 September 2024

PUBLISHED
27 September 2024

PAPER

Band alignments, conduction band edges and intralayer bandgap renormalisation in $MoSe_2/WSe_2$ heterobilayers

A J Graham[1], P V Nguyen[2], H Park[2], J Nunn[1], V Kandyba[3], M Cattelan[3], A Giampietri[3], A Barinov[3], X Xu[2,4,*], D H Cobden[2,*] and N R Wilson[1,*]

1 Department of Physics, University of Warwick, Coventry CV4 7AL, United Kingdom
2 Department of Physics, University of Washington, Seattle, WA, United States of America
3 Elettra—Sincrotrone Trieste, S.C.p.A, Basovizza, TS 34149, Italy
4 Department of Materials Science and Engineering, University of Washington, Seattle, WA, United States of America
* Authors to whom any correspondence should be addressed.

E-mail: xuxd@uw.edu, cobden@uw.edu and neil.wilson@warwick.ac.uk

Keywords: angle resolved photoemission spectroscopy, heterobilayers, transition metal dichalcogenides, electronic structure, 2D heterostructures

Supplementary material for this article is available online

Abstract

Stacking two semiconducting transition metal dichalcogenide (MX_2) monolayers to form a heterobilayer creates a new variety of semiconductor junction with unique optoelectronic features, such as hosting long-lived dipolar interlayer excitons. Despite many optical, transport, and theoretical studies, there have been few direct electronic structure measurements of these junctions. Here, we apply angle-resolved photoemission spectroscopy with micron-scale spatial resolution (μARPES) to determine the band alignments in $MoSe_2/WSe_2$ heterobilayers, using *in-situ* electrostatic gating to electron-dope and thus probe the conduction band edges. By comparing spectra from heterobilayers with opposite stacking orders, that is, with either $MoSe_2$ or WSe_2 on top, we confirm that the band alignment is type II, with the valence band maximum in the WSe_2 and the conduction band minimum in the $MoSe_2$. The overall band gap is $E_G = 1.43 \pm 0.03$ eV, and to within experimental uncertainty it is unaffected by electron doping. However, the offset between the WSe_2 and $MoSe_2$ valence bands clearly decreases with increasing electron doping, implying band renormalisation only in the $MoSe_2$, the layer in which the electrons accumulate. In contrast, μARPES spectra from a $WS_2/MoSe_2$ heterobilayer indicate type I band alignment, with both band edges in the $MoSe_2$. These insights into the doping-dependent band alignments and gaps of MX_2 heterobilayers will be useful for properly understanding and ultimately utilizing their optoelectronic properties.

1. Introduction

Monolayers of the 2D semiconducting transition metal dichalcogenides of formula MX_2, where M = Mo or W and X = S or Se, have direct band gaps at the Brillouin zone corners (**K**-points) and spin-polarised band edges [1, 2] suggesting valleytronic and spintronic applications [3, 4]. Stacking two different MX_2 monolayers to form a heterobilayer can create a type II (staggered gap) semiconductor junction where the valence band maximum (VBM) and conduction band minimum (CBM) reside in opposite layers [5, 6]. This situation supports long-lived interlayer excitons (IXs), where the hole and electron are localised on opposite layers [7–9]. Further interest in MX_2 heterobilayers has been driven by the observation of IXs trapped in the moiré superlattice potential arrays formed due to the crystal mismatch [10–14]. However, experimental measurements of the momentum-resolved electronic structure of these heterobilayers are scarce [15–20], and uncertainty remains over the vital question of band alignments, particularly at the conduction band edge. For example, in the $MoSe_2/WSe_2$ heterobilayer, which has been widely studied as a host of IXs [8], the lowest energy IX has been reported in some studies to be the **K-Q** exciton [21, 22] and in others to be the **K-K** exciton [23], indicating confusion over whether the CBM is at **Q** or **K**.

Angle-resolved photoemission spectroscopy with micrometre-scale spatial resolution (μARPES) is a powerful tool for directly probing the valence band structure of two-dimensional materials and heterostructures [23–29]. Combining μARPES with *in-situ* electrostatic gating [30–33] allows the study of conduction band edges in 2D semiconductor heterostructures [20] and has demonstrated the significance of band gap renormalisation with increasing carrier concentration in monolayer MX_2 [33]. Here, we use this approach to determine band alignments and band gaps of $MoSe_2/WSe_2$ heterobilayers, resolving the question of the position of the CBM and also observing gate-dependent electronic structure changes.

2. Results and discussion

Two $MoSe_2/WSe_2$ heterobilayer devices, with opposite stacking orders, were fabricated using mechanical exfoliation and dry transfer techniques (see Methods). The devices are essentially capacitors: a graphene sheet (top electrode) overlaps the MX_2 heterobilayer, separated by an hBN flake (dielectric) from a bottom graphite electrode supported on an SiO_2/Si substrate. Platinum contacts allow a gate voltage, V_G, to be applied to the graphite while the graphene is grounded through a current preamplifier, in order to electrostatically dope the MX_2. A schematic of the design is shown in the supplementary information (SI section 1) along with optical, atomic force and scanning photoemission microscopy images of device 1 and device 2. From constant-energy maps (SI section 2), we deduce that in device 1 ($MoSe_2$ on top) the twist angle between the layers is close to 0° and in device 2 (WSe_2 on top) it is $6 \pm 1°$.

Energy–momentum slices without electrostatic doping (i.e. at $V_G = 0$) are shown in figure 1(a) (for device 1) and (b) (for device 2). The intensities of similar features in the two devices are very different. This is explained by the higher probability of photoelectron escape from the topmost layer, so that bands with more orbital weight in that layer are more intense. Near $\mathbf{\Gamma}$, strong intensity is seen from the upper valence bands near $\mathbf{\Gamma}$ in both devices, reflecting hybridization between the layers of the metal d_{z^2}-like states near $\mathbf{\Gamma}$ [1]. Near **K**, on the other hand, for $MoSe_2$ on top (device 1, figure 1(a)) the two spin-split valence bands from the $MoSe_2$ (fitted by green dotted lines) are stronger, while for WSe_2 on top (device 2, figure 1(b)) the corresponding valence bands from the WSe_2 (purple dotted lines) are stronger. Along with dispersion that matches the bands in the isolated monolayers (SI section 1), this reflects negligible hybridization of the metal $d_{x^2-y^2}$-like states near **K** [34]. Note that the lower bands near **K** in the $MoSe_2$ and the WSe_2 are almost coincident, and whichever is stronger masks the other.

The valence band parameters determined from the fits are summarised in table 1. The overall VBM is at $\mathbf{K}_{WSe2}$, as expected [23]. For device 1 we can determine a valence band offset of $E_{K_1} - E_{K_2} = 0.31 \pm 0.04$ eV relative to the $MoSe_2$ valence band at $\mathbf{K}_{MoSe2}$, and the energy separation between the two bands at $\mathbf{\Gamma}$ is $E_\Gamma - E_K = 0.67 \pm 0.04$ eV. The measured band parameters are consistent between the different stacking orders and twist angles.

Electrostatically doping the heterobilayer populates the conduction band, making it visible in the μARPES spectra. Figures 1(c) and (d) show μARPES energy–momentum slices at $V_G = +4$ V for the $MoSe_2/WSe_2$ and $WSe_2/MoSe_2$ heterobilayers, respectively; with similar hBN dielectric thicknesses (device 1 hBN thickness $= 9.4 \pm 0.5$ nm, device 2 hBN thickness $= 9 \pm 1$ nm), the electron concentrations in both spectra are $\sim 10^{13}$ cm^{-2}. For both stacking orders, the CBM is observed in the $MoSe_2$ layer at $\mathbf{K}_{MoSe2}$, establishing a type II band alignment in agreement with optical measurements [8, 23]. From these spectra, the band gaps for $MoSe_2/WSe_2$ and $WSe_2/MoSe_2$ are found to be identical at 1.42 ± 0.04 eV and 1.43 ± 0.03 eV, respectively. The IX emission peak in $MoSe_2/WSe_2$ heterobilayers varies in the range 1.3–1.4 eV depending on the twist angle and temperature [7, 8, 23, 35 36]. The observed gap of 1.43 eV is thus consistent with an IX binding energy of around 100 meV, as predicted for $WSe_2/MoSe_2$ heterobilayers in this dielectric environment [37].

Weak photoemission intensity is also observed around the Fermi energy, E_F, at $\mathbf{Q}_{MoSe2}$ in figures 1(c) and (d), although with significantly lower intensity when the WSe_2 is on top in figure 1(d). This shows that the CBM at $\mathbf{Q}_{MoSe2}$ is close in energy to the CBM at $\mathbf{K}_{MoSe2}$. To estimate the energy offset, E_{KQ}, between **K** and **Q**, measurements were made at multiple gate voltages on device 1, as shown in figure 2. The lowest gate voltage at which photoemission is observed at the CBM at $\mathbf{K}_{MoSe2}$ is +1.2 V, in agreement with the onset of a measurable photocurrent (SI section 3). (Note that the low intensity band approximately 0.5 eV above the valence band in this spectrum is from an un-gated region of the sample within the beam spot, contributing some spectral intensity at reduced binding energy.) At $V_G = +3$ V, photoemission from the conduction band at $\mathbf{Q}_{MoSe2}$ becomes visible. Assuming that the chemical potential in the heterobilayer is aligned with the CBM at **K** at $V_G = +1.2$ V and with the band minimum at **Q** at +3.0 V, from the shift in chemical potential between these two gate voltages we find $E_{KQ} = 15 \pm 4$ meV (see methods and SI section 4). This is less than expected for an isolated $MoSe_2$ monolayer, where *ab initio* calculations predict $E_{KQ} \sim 150$ meV [34], and may

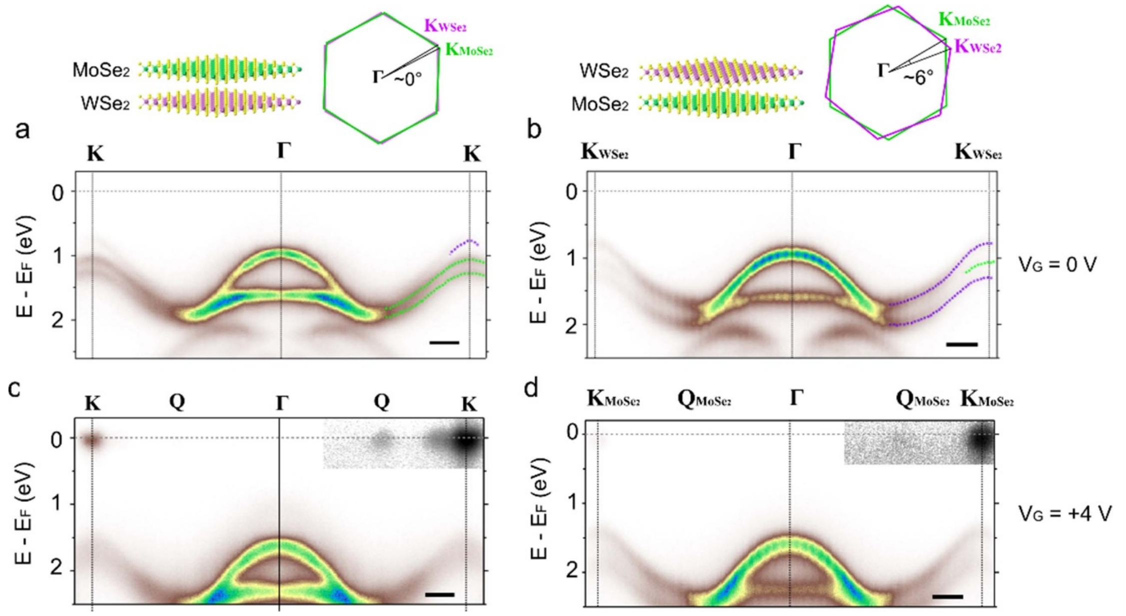

Figure 1. $MoSe_2/WSe_2$ and $WSe_2/MoSe_2$ heterobilayer band alignments. Left, μARPES measurements on device 1 with $MoSe_2$ on top and twist angle 0°; right, measurements on device 2 with WSe_2 on top and twist angle 6° (a) and (b), energy–momentum slices at zero gate voltage along the high symmetry lines indicated in the Brillouin zones shown above. Overlaid dotted green and purple lines mark bands originating from the $MoSe_2$ and WSe_2 layers respectively. (c) and (d), Corresponding measurements at gate voltage +4 V. The data is mirrored across **Γ** in each case, and a logarithmic map (grayscale) is used to reveal weaker conduction band features. Scale bars are 0.2 Å^{-1}.

Table 1. Band parameters of $MoSe_2/WSe_2$ heterobilayers and monolayers. E_K is the energy of the uppermost band edge at **K**, $E_\Gamma - E_K$ is the energy difference between the uppermost band at **Γ** and at **K**, $E_{K_1} - E_{K_2}$ is the valence band offset between the band edges of the $MoSe_2$ and WSe_2 layers at **K**, Δ_Γ is the energy separation of the bands at Γ, Δ_{SO} is the spin–orbit splitting and m^* is the effective mass of the bands at **K**, found from a parabolic fit in a symmetric window of 0.1 Å^{-1}. The monolayer band parameters are from monolayer regions measured on device 1.

	E_K (eV)	$E_\Gamma - E_K$ (eV)	$E_{K_1} - E_{K_2}$ (eV)	Δ_Γ (eV)	$\Delta^{SO}_{MoSe_2}$ (eV)	$\Delta^{SO}_{WSe_2}$ (eV)	$m^*_{MoSe_2}$ (m_0)	$m^*_{WSe_2}$ (m_0)
$MoSe_2/WSe_2$ Device 1: 0°	0.74 ± 0.03	0.23 ± 0.04	0.31 ± 0.04	0.67 ± 0.04	0.21 ± 0.04	—	0.7 ± 0.1	0.4 ± 0.1
$WSe_2/MoSe_2$ Device 2: 6°	0.78 ± 0.03	0.17 ± 0.04	0.28 ± 0.04	0.65 ± 0.04	—	0.52 ± 0.04	1.0 ± 0.2	0.4 ± 0.1
Monolayer $MoSe_2$	1.18 ± 0.03	0.46 ± 0.04	—	—	0.18 ± 0.04	—	0.6 ± 0.1	—
MonolayerWSe_2	0.81 ± 0.03	0.64 ± 0.04	—	—	—	0.49 ± 0.04	—	0.4 ± 0.1

indicate hybridisation between the layers. At **Q**, the orbital composition includes contributions from the chalcogen p_z orbitals [1] which result in significant changes in the band edge energy in multilayers. For TMD homobilayers, the local minima at **Q** become the CBM [33], while in the $MoSe_2/WSe_2$ heterobilayer the CBM remains at **K** but with a reduced offset E_{KQ}.

In the spectra acquired at $V_G = +2$ and +4 V, a single 'replica' of the CBM is visible in the μARPES spectra around E_F (see also SI section 5) and close to **K** (in device 1, $\mathbf{K}_{Mose2}$ and $\mathbf{K}_{WSe2}$ are co-located to within experimental resolution). Such replicas can be caused by final-state diffraction of the photo-emitted electrons [20, 38–42] and/or by modification of the initial state by the moiré superlattice potential. We note that the replica band is only apparent in the spectra taken at $V_G = +2$ and +4 V, and attribute this variability to small shifts of the beam spot position on the sample between gate voltages (see Methods). Distinguishing the origin of the replicas is not trivial and our data is not conclusive here: further work is required to investigate possible moiré effects in the electronic structure of these $MoSe_2/WSe_2$ heterobilayers.

Increasing the electron doping in the $MoSe_2/WSe_2$ heterobilayer causes a noticeable change in the bands [33, 43]. Figure 3(a) shows energy distribution curves (EDCs) extracted at **K** from the μARPES spectra in figures 1 and 2 for device 1. The conduction band peak is fit using a product of a Gaussian function and a broadened Fermi–Dirac distribution (SI section 6). Three peaks in photoemission intensity can be resolved on the valence side: the VBM from the WSe_2 layer, and the two spin-split $MoSe_2$ bands. As V_G is increased beyond +1.2 V, the $MoSe_2$ valence bands at **K** move up in energy, reducing the valence band offset between the $MoSe_2$ and WSe_2. From the fits both the overall band gap, E_G,

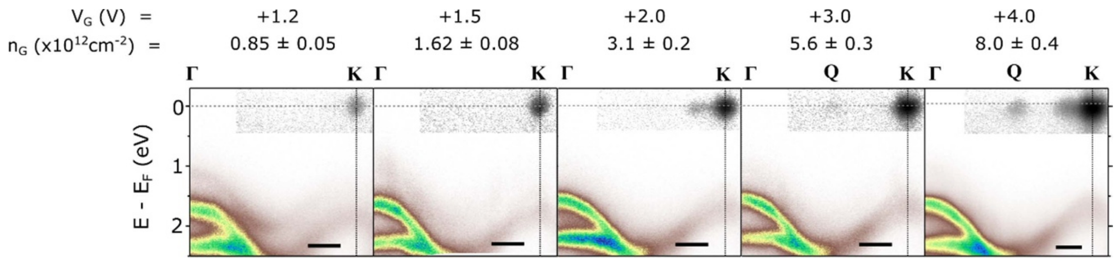

Figure 2. Gate-dependent μARPES spectra of the $MoSe_2/WSe_2$ heterobilayer. μARPES energy–momentum slices along the **Γ** to **K** direction acquired at the indicated gate voltages, V_G, and carrier concentrations, n_G, in device 1. Data shown in grayscale are in logarithmic scale. Scale bars are 0.2 Å^{-1}.

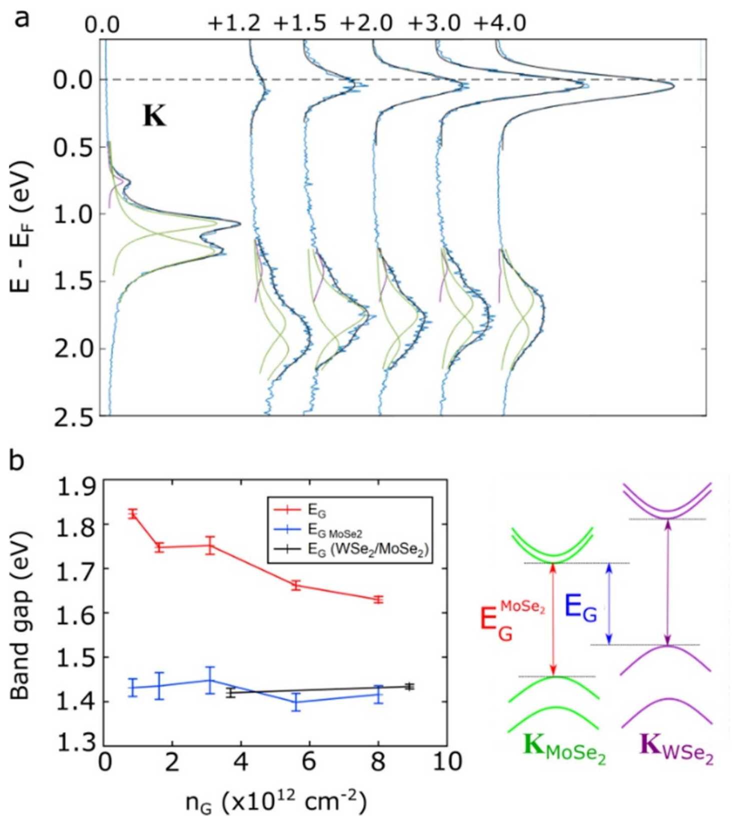

Figure 3. Intralayer band renormalisation in $MoSe_2/WSe_2$ heterobilayer. (a) Energy distribution curves (EDCs) taken at **K** from the spectra shown in Figures 1(a) and 2. The gate voltage is specified above each EDC. The black lines overlaid on the data are fits including the conduction and valence bands. The purple and green profiles under each EDC show the contributions of the WSe_2 VBM and the two spin-split $MoSe_2$ bands, respectively. (b) Variation with electron doping n_G of the $MoSe_2$ intralayer band gap E_G^{MoSe2} (red), the $MoSe_2/WSe_2$ heterobilayer overall band gap E_G (blue), and the $WSe_2/MoSe_2$ heterobilayer overall gap (black). These quantities are defined in the schematic to the right.

and the intralayer band gap of the $MoSe_2$, $E_G{}^{MoSe2}$, can be determined, as shown in figure 3(b). While E_G remains constant at 1.43 ± 0.03 eV, $E_G{}^{MoSe2}$ decreases by roughly 0.2 eV, from 1.82 ± 0.01 eV at $n_G = 0.85 \times 10^{12}$ cm^{-2} to 1.64 ± 0.01 eV at 8.0×10^{12} cm^{-2}. For device 2, with the reverse stacking order, we similarly find that E_G is independent of doping. Application of an electric field across the heterobilayer changes the exciton binding energy as well as the band alignments, complicating direct comparison of the gate-dependence of the band gap with IX emission. Over the range of electric field achieved here, the IX emission should Stark shift by $\leqslant$50 meV [8, 44], comparable with our measurement resolution. Higher resolution μARPES will thus be required to probe the corresponding Stark shift of the direct gap.

The fact that doping renormalizes the valence bands derived from the $MoSe_2$ but not those from the WSe_2 requires theoretical attention, but suggests that electrons localized in the $MoSe_2$ layer screen Coulomb interactions in the $MoSe_2$ more strongly than in the WSe_2. As a result, on doping, the type II staggered band gap is retained, with the VBM remaining at $\mathbf{K}_{WSe2}$ and the CBM at $\mathbf{K}_{MoSe2}$. For small twist angles this leads to an almost-direct gap, consistent with the strong photoluminescence observed from recombination of IX in such samples. We remark that no measurable effect of V_G can be seen on the separation of the bands at $\mathbf{\Gamma}$, implying that the hybridisation between the $MoSe_2$ and WSe_2 layers is insensitive to electric field.

Finally, we note that not all MX_2 heterobilayers have unambiguous type II band alignment. For example, gate dependent μARPES spectra from a $WS_2/MoSe_2$ heterobilayer are shown in SI section 7. The VBM is at $\mathbf{K}_{MoSe2}$, as expected from optical spectroscopy [13, 45–48], but the valence band edge at $\mathbf{\Gamma}$ is very close, with $E_{K\Gamma} = 0.06 \pm 0.1$ eV, and the conduction band edges at $\mathbf{K}_{MoSe2}$ and $\mathbf{K}_{WS2}$ are nearly degenerate, the difference being below our measurement resolution. From their relative photoemission intensity, it appears that the CB at $\mathbf{K}_{MoSe2}$ is marginally lower, but the electron doping is substantially shared between the layers. Close energy alignment of the conduction band edges is consistent with the observations of resonantly hybridised excitons [13, 49] and fast interlayer energy transfer [47] in $MoSe_2/WS_2$ heterobilayers.

3. Conclusions

In conclusion, μARPES measurements affirm a type II staggered gap in $MoSe_2/WSe_2$ heterobilayers and yield momentum-resolved valence and conduction band alignments. On electron doping, intralayer band renormalisation is seen in the $MoSe_2$-derived bands, yet the net band gap does not change. This presents an interesting counterpoint to other 2D semiconductor heterostructures where electron doping causes a substantial reduction of the band gap [33, 50, 51].

4. Methods

4.1. Sample fabrication

Heterobilayers were fabricated by mechanical exfoliation and dry transfer using a polycarbonate film, as described previously [33]. The back gate is formed from hBN on graphite, with the hBN thin (around 10 nm) to minimise the photocurrent generated by the x-ray beam when a gate voltage is applied, and transferred onto substrates with electrodes (Pt/Ti, 30 nm/5 nm) predefined by electron beam lithography, making a contact to the graphite gate electrode. MX_2 monolayers are then exfoliated, identified, aligned and transferred onto the gate structure. Finally, a graphene flake is transferred to make a top contact, partially covering the MX_2 heterobilayer. It is important to provide effective dissipation of the photocurrent during μARPES of semiconducting samples, particularly during in situ gating. To do this, measurements were acquired with the beam spot close to the graphene electrodes and, for some samples, the graphene top contact was pre-patterned into a comb-like structure using nanolithography by atomic force microscopy [52]. Although we do not expect graphene to make an Ohmic contact to the MX_2 due to the significant conduction and valence band offsets between MX_2 and graphene [23], the contact resistance is low enough given the small photocurrents [33] and the transfer of graphene allows a clean top surface with minimal damage more easily than lithographically defined metal contacts. As described previously [33], the samples were mounted in a chip carrier to allow electrical contact connection during ARPES. Spectra from three different samples are reported here: device 1, monolayer $MoSe_2$ on WSe_2 with hBN thickness $= 9.4 \pm 0.5$ nm; device 2, monolayer WSe_2 on $MoSe_2$ with hBN thickness $= 9 \pm 1$ nm; and device 3, monolayer WS_2 on $MoSe_2$ with hBN thickness $= 5.5 \pm 0.5$ nm. The twist angles were determined to an uncertainty of $\pm 1^\circ$ by fitting the peak intensities in the constant energy maps at the VBM/CBM corresponding to the different layers.

4.2. μARPES with *in-situ* electrostatic gating

μARPES measurements were performed on the SPECTROMICROSCOPY beamline at the Elettra synchrotron in Italy [53]. Linearly polarised light was incident on the sample surface at an angle of 45° with a photon energy of 27 eV, focused to a spot size of roughly 600 nm. The region of interest was located using scanning photoemission microscopy. The photon beam was then positioned on the region of interest and three-dimensional μARPES intensity maps $I(E, k_x, k_y)$ were acquired by collecting a series of 2D detector images. μARPES energy–momentum slices were extracted from the resulting three-dimensional datasets by interpolating between detector slices. A gate voltage was applied, and the photocurrent measured, using a Keithley 487 Picoammeter connected to contact pins located at the bottom of the sample plate inside the chamber. The measured sample temperature during μARPES acquisition was 80 K, thermal drift of the sample during measurement was typically much less than 1 μm per hour. Prior to measurement, samples were annealed in ultra-high vacuum for approximately 8 h at 650 K.

4.3. Determining carrier concentrations, conduction band positions and alignments

For small values of V_G, the chemical potential lies within the band gap of the semiconductor and the bands shift linearly and electrostatically. At a threshold gate voltage, the CBM of the semiconductor aligns with the Fermi energy of the graphene (ground) contact and the semiconductor starts to conduct, with the spectral intensity from the valence bands shifting back to a higher energy as described in [33]. From this point on, due to the large density of states in the conduction band, the chemical potential rises relative to the conduction band edge much more slowly with V_G as electrons accumulate. The further increase in the electric field in the hBN that controls the electron doping, n_G, is determined by $V_G - \Delta E_\Gamma$, where the shift, ΔE_Γ, is directly measured from the μARPES spectra at $\boldsymbol{\Gamma}$. SI figures S3(a) and (b) show how ΔE_Γ and $V_G - \Delta E_\Gamma$ change with V_G for device 1. The doping is then calculated using $n_G = \frac{C}{e}\left|\left(V_G - \frac{\Delta E_\Gamma}{e}\right)\right|$ where $C = \frac{\varepsilon_{hBN}\varepsilon_0}{d_{hBN}}$, with $\varepsilon_{hBN} = 4.0$ [33] the dielectric constant of hBN, and d_{hBN} the hBN thickness. The energy difference between the chemical potential and the CBM, or $E_F - E_C$, is finally deduced from the density of states of the conduction band and the Fermi–Dirac distribution, F(E), using $n_G = \int_{E_C}^{\infty} F(E)\, g_{2D} dE$.

For a 2D parabolic band $g_{2D} = \frac{g_s g_v m_e^*}{\pi \hbar^2}$, where g_s is the spin degeneracy, g_v is the valley degeneracy and m_e^* is the electron effective mass. For the $MoSe_2/WSe_2$ heterobilayer, three 2D parabolic bands in the $MoSe_2$ conduction band must be considered. Therefore, to calculate the value of $E_F - E_C$ for each carrier concentration the following equation is used:

$$n_G = k_B T \left[g_{K1} \ln\left(1 + \exp\left[\frac{(E_F - E_C)}{k_B T}\right]\right) + g_{K2} \ln\left(1 + \exp\left[\frac{E_F - (E_C + \Delta_{SO})}{k_B T}\right]\right) + g_Q \ln\left(1 + \exp\left[\frac{E_F - (E_C + E_{QK})}{k_B T}\right]\right)\right],$$

where Δ_{SO} is the spin-splitting at $\mathbf{K}$ in the $MoSe_2$ conduction band and g_{K1}, g_{K2} and g_Q are the densities of states of the two spin-split bands at $\mathbf{K}$ and at $\mathbf{Q}$, respectively. Tabulated in SI table S2 are the values found for $E_F - E_C$ for each carrier concentration. The parameters used to calculate $E_F - E_C$ were $m^*_K = 0.57\ m_0$ [34], $m^*_Q = 0.80\ m_0$ [54], $\Delta_{SO} = 20$ meV [34], $E_{QK} = 15.1$ meV and $T = 80$ K.

E_{KQ} is determined from the change in E_F between $V_G = +1.2$ V and +3 V. SI section 4 explains how the change in chemical potential between +1.2 and +3 V is found from the calculated carrier concentration and $E_F - E_C$. As the value of $E_F - E_C$ depends on E_{KQ}, E_{KQ} is varied in $n_G = \int_{E_C}^{\infty} F(E)\, g_{2D} dE$ until $E_F - E_C$ is equal to the change in chemical potential between +1.2 and +3 V.

4.4. Fitting the CBM

The peak in photoemission intensity from the CBM in each of gated μARPES spectrum is fitted with a product of a Gaussian and sigmoid function, where the sigmoid function represents the Fermi–Dirac distribution. $E_F - E_C$ is fixed in the fit to the values calculated using the equation, $n_G = \int_{E_C}^{\infty} F(E)\, g_{2D} dE$ (values listed in SI table S2). For each gate voltage the fits of the CBM are shown in SI section 6.

Data availability statement

The research data supporting this publication can be accessed from the corresponding authors upon reasonable request.

The data that support the findings of this study are openly available at the following URL/DOI: https://wrap.warwick.ac.uk/187279/ [55].

Acknowledgment

Research on ARPES of MX_2 heterobilayers at UW was solely supported by Programmable Quantum Materials, an Energy Frontier Research Center funded by the U.S. Department of Energy (DOE), Office of Science, Basic Energy Sciences (BES), under award DE-SC0019443. NRW was supported by EPSRC (Grants EP/T027207/1, EP/P01139X/1 and EP/R513374/1). J N was funded by Diamond Light Source and the University of Warwick. For device fabrication, facilities were used that are supported by the National Science Foundation (NSF) through the UW Molecular Engineering Materials Center (MEM-C), a Materials Research Science and Engineering Center (DMR- 2308979).

ORCID iDs

H Park https://orcid.org/0000-0002-3895-9589
N R Wilson https://orcid.org/0000-0002-2592-3077

References

[1] Liu G-B, Xiao D, Yao Y, Xu X and Yao W 2015 Electronic structures and theoretical modelling of two-dimensional group-VIB transition metal dichalcogenides *Chem. Soc. Rev.* **44** 2643–63
[2] Manzeli S, Ovchinnikov D, Pasquier D, Yazyev O V and Kis A 2017 2D transition metal dichalcogenides *Nat. Rev. Mater.* **2** 17033
[3] Schaibley J R, Yu H, Clark G, Rivera P, Ross J S, Seyler K L, Yao W and Xu X 2016 Valleytronics in 2D materials *Nat. Rev. Mater.* **1** 16055
[4] Liu Y, Gao Y, Zhang S, He J, Yu J and Liu Z 2019 Valleytronics in transition metal dichalcogenides materials *Nano Res.* **12** 2695–711
[5] Kang J, Tongay S, Zhou J, Li J and Wu J 2013 Band offsets and heterostructures of two-dimensional semiconductors *Appl. Phys. Lett.* **102** 012111
[6] Komsa H-P and Krasheninnikov A V 2013 Electronic structures and optical properties of realistic transition metal dichalcogenide heterostructures from first principles *Phys. Rev.* B **88** 085318

[7] Rivera P, Yu H, Seyler K L, Wilson N P, Yao W and Xu X 2018 Interlayer valley excitons in heterobilayers of transition metal dichalcogenides *Nat. Nanotechnol.* **13** 1004–15
[8] Rivera P *et al* 2015 Observation of long-lived interlayer excitons in monolayer $MoSe_2$-WSe_2 heterostructures *Nat. Commun.* **6** 6242
[9] Mak K F and Shan J 2018 Opportunities and challenges of interlayer exciton control and manipulation *Nat. Nanotechnol.* **13** 974–6
[10] Seyler K L, Rivera P, Yu H, Wilson N P, Ray E L, Mandrus D G, Yan J, Yao W and Xu X 2019 Signatures of moiré-trapped valley excitons in $MoSe_2/WSe_2$ heterobilayers *Nature* **567** 66–70
[11] Tran K *et al* 2019 Evidence for moiré excitons in van der Waals heterostructures *Nature* **567** 71–75
[12] Huang D, Choi J, Shih C-K and Li X 2022 Excitons in semiconductor moiré superlattices *Nat. Nanotechnol.* **17** 227–38
[13] Zhang L *et al* 2020 Twist-angle dependence of moiré excitons in $WS_2/MoSe_2$ heterobilayers *Nat. Commun.* **11** 5888
[14] Yu H, Liu G-B, Tang J, Xu X and Yao W 2017 Moiré excitons: from programmable quantum emitter arrays to spin-orbit–coupled artificial lattices *Sci. Adv.* **3** e1701696
[15] Khalil L *et al* 2023 Hybridization and localized flat band in the $WSe_2/MoSe_2$ heterobilayer *Nanotechnology* **34** 045702
[16] Karni O *et al* 2022 Structure of the moiré exciton captured by imaging its electron and hole *Nature* **603** 247–52
[17] Schmitt D *et al* 2022 Formation of moiré interlayer excitons in space and time *Nature* **608** 499–503
[18] Xie S *et al* 2022 Strong interlayer interactions in bilayer and trilayer moiré superlattices *Sci. Adv.* **8** 4–10
[19] Jones A J H *et al* 2022 Visualizing band structure hybridization and superlattice effects in twisted MoS_2 /WS_2 heterobilayers *2D Mater.* **9** 015032
[20] Graham A J *et al* 2024 Conduction band replicas in a 2D moiré semiconductor heterobilayer *Nano Lett.* **24** 5117–24
[21] Miller B, Steinhoff A, Pano B, Klein J, Jahnke F, Holleitner A and Wurstbauer U 2017 Long-lived direct and indirect interlayer excitons in van der Waals heterostructures *Nano Lett.* **17** 5229–37
[22] Barré E *et al* 2022 Optical absorption of interlayer excitons in transition-metal dichalcogenide heterostructures *Science* **376** 406–10
[23] Wilson N R *et al* 2017 Determination of band offsets, hybridization, and exciton binding in 2D semiconductor heterostructures *Sci. Adv.* **3** e1601832
[24] Cucchi I, Lisi S, Margot F, Henck H, Tamai A and Baumberger F 2021 Electronic structure of 2D van der Waals crystals and heterostructures investigated by spatially- and angle-resolved photoemission *C. R. Phys.* **22** 107–31
[25] Coy Diaz H, Avila J, Chen C, Addou R, Asensio M C and Batzill M 2015 Direct observation of interlayer hybridization and Dirac relativistic carriers in graphene/MoS_2 van der Waals heterostructures *Nano Lett.* **15** 1135–40
[26] Ulstrup S *et al* 2020 Direct observation of minibands in a twisted graphene/WS_2 bilayer *Sci. Adv.* **6** 1–7
[27] Lisi S *et al* 2020 Observation of flat bands in twisted bilayer graphene *Nat. Phys.* **17** 189–94
[28] Utama M I B *et al* 2021 Visualization of the flat electronic band in twisted bilayer graphene near the magic angle twist *Nat. Phys.* **17** 184–8
[29] Margot F *et al* 2023 Electronic structure of few-layer black phosphorus from μ-ARPES *Nano Lett.* **23** 6433–9
[30] Joucken F *et al* 2019 Visualizing the effect of an electrostatic gate with angle-resolved photoemission spectroscopy *Nano Lett.* **19** 2682–7
[31] Nguyen P V *et al* 2021 Field-dependent band structure measurements in two-dimensional heterostructures *Nano Lett.* **21** 10532–7
[32] Jones A J H H *et al* 2020 Observation of electrically tunable van hove singularities in twisted bilayer graphene from NanoARPES *Adv. Mater.* **32** 2001656
[33] Nguyen P V *et al* 2019 Visualizing electrostatic gating effects in two-dimensional heterostructures *Nature* **572** 220–3
[34] Kormányos A, Burkard G, Gmitra M, Fabian J, Zólyomi V, Drummond N D and Fal'ko V 2015 k p theory for two-dimensional transition metal dichalcogenide semiconductors *2D Mater.* **2** 022001
[35] Nayak P K *et al* 2017 Probing evolution of twist-angle-dependent interlayer excitons in $MoSe_2/WSe_2$ van der Waals heterostructures *ACS Nano* **11** 4041–50
[36] Nagler P *et al* 2017 Interlayer exciton dynamics in a dichalcogenide monolayer heterostructure *2D Mater.* **4** 025112
[37] Kamban H C and Pedersen T G 2020 Interlayer excitons in van der Waals heterostructures: binding energy, Stark shift, and field-induced dissociation *Sci. Rep.* **10** 36–40
[38] Ohta T, Robinson J T, Feibelman P J, Bostwick A, Rotenberg E and Beechem T E 2012 Evidence for interlayer coupling and moiré periodic potentials in twisted bilayer graphene *Phys. Rev. Lett.* **109** 186807
[39] Pletikosić I, Kralj M, Pervan P, Brako R, Coraux J, N'Diaye A T, Busse C and Michely T 2009 Dirac cones and minigaps for graphene on Ir(111) *Phys. Rev. Lett.* **102** 056808
[40] Starodub E, Bostwick A, Moreschini L, Nie S, Gabaly F, McCarty E, K F and Rotenberg E 2011 In-plane orientation effects on the electronic structure, stability, and Raman scattering of monolayer graphene on Ir(111) *Phys. Rev.* B **83** 125428 (available at: https://journals.aps.org/prb/abstract/10.1103/PhysRevB.83.125428)
[41] Rotenberg E and Bostwick A 2015 Superlattice effects in graphene on SiC(0001) and Ir(111) probed by ARPES *Synth. Met.* **210** 85–94
[42] Wallbank J R, Fal'ko V and Mucha-Kruczynski M 2016 Moiré miniband features in the angle-resolved photoemission spectra of graphene/ h BN heterostructures *Phys. Rev.* B **93** 085409 (available at: https://journals.aps.org/prb/abstract/10.1103/PhysRevB.93.085409)
[43] Gao S and Yang L 2017 Renormalization of the quasiparticle band gap in doped two-dimensional materials from many-body calculations *Phys. Rev.* B **96** 155410
[44] Ciarrocchi A, Unuchek D, Avsar A, Watanabe K, Taniguchi T and Kis A 2019 Polarization switching and electrical control of interlayer excitons in two-dimensional van der Waals heterostructures *Nat. Photonics* **13** 131–6
[45] Tang Y, Gu J, Liu S, Watanabe K, Taniguchi T, Hone J, Mak K F and Shan J 2021 Tuning layer-hybridized moiré excitons by the quantum-confined Stark effect *Nat. Nanotechnol.* **16** 52–57
[46] Zhang L, Wu F, Hou S, Zhang Z, Chou Y-H, Watanabe K, Taniguchi T, Forrset S R and Deng H 2021 Van der Waals heterostructure polaritons with moiré-induced nonlinearity *Nature* **591** 61–65 (available at: https://www.nature.com/articles/s41586-021-03228-5)
[47] Kozawa D, Carvalho A, Verzhbitskiy I, Giustiniano F, Miyauchi Y, Mouri S, Castro Neto A H, Matsuda K and Eda G 2016 Evidence for fast interlayer energy transfer in $MoSe_2/WS_2$ heterostructures *Nano Lett.* **16** 4087–93
[48] Meng Y, Wang T, Jin C, Li Z, Miao S, Lian Z, Taniguchi T, Watanabe K, Song F and Shi S F 2020 Electrical switching between exciton dissociation to exciton funneling in $MoSe_2/WS_2$ heterostructure *Nat. Commun.* **11** 2640 (available at: https://www.nature.com/articles/s41467-020-16419-x)
[49] Alexeev E M *et al* 2019 Resonantly hybridized excitons in moiré superlattices in van der Waals heterostructures

Nature **567** 81–86 (available at: https://www.nature.com/articles/s41586-019-0986-9)

[50] Qi J, Li X, Qian X and Feng J 2013 Bandgap engineering of rippled MoS_2 monolayer under external electric field *Appl. Phys. Lett.* **102** 173112

[51] Liu Y, Qiu Z, Carvalho A, Bao Y, Xu H, Tan S J R, Liu W, Castro Neto A H, Loh K P and Lu J 2017 Gate-tunable giant Stark effect in few-layer black phosphorus *Nano Lett.* **17** 1970–7

[52] Li H, Ying Z, Lyu B, Deng A, Wang L, Taniguchi T, Watanabe K and Shi Z 2018 Electrode-free anodic oxidation nanolithography of low-dimensional materials *Nano Lett.* **18** 8011–5

[53] Dudin P, Lacovig P, Fava C, Nicolini E, Bianco A, Cautero G and Barinov A 2010 Angle-resolved photoemission spectroscopy and imaging with a submicrometre probe at the SPECTROMICROSCOPY-3.2L beamline of elettra *J. Synchrotron. Radiat.* **17** 445–50

[54] Wang J, Ardelean J, Bai Y, Steinhoff A, Florian M, Jahnke F, Xu X, Kira M, Hone J and Zhu X Y 2019 Optical generation of high carrier densities in 2D semiconductor heterobilayers *Sci. Adv.* **5** 2–10

[55] Graham A J *et al* 2024 Band alignments, conduction band edges and intralayer bandgap renormalisation in MoSe2/WSe2 heterobilayers (available at: https://wrap.warwick.ac.uk/187279/)